Journal of Solid State Chemistry 182 (2009) 2716–2724

Contents lists available at ScienceDirect

Journal of Solid State Chemistry

journal homepage: www.elsevier.com/locate/jssc

Synthesis and characterization of monodisperse spherical $SiO_2@RE_2O_3$ (RE = rare earth elements) and $SiO_2@Gd_2O_3:Ln^{3+}$ (Ln = Eu, Tb, Dy, Sm, Er, Ho) particles with core-shell structure

H. Wang, J. Yang, C.M. Zhang, J. Lin *

State Key Laboratory of Rare Earth Resource Utilization, Changchun Institute of Applied Chemistry, Chinese Academy of Sciences, Changchun 130022, PR China

ARTICLE INFO

Article history:
Received 23 February 2009
Received in revised form
10 July 2009
Accepted 18 July 2009
Available online 24 July 2009

Keywords:
Silica
Rare earth elements
Core-shell
Luminescence

ABSTRACT

Spherical SiO_2 particles have been coated with rare earth oxide layers by a Pechini sol–gel process, leading to the formation of core-shell structured $SiO_2@RE_2O_3$ (RE = rare earth elements) and $SiO_2@Gd_2O_3:Ln^{3+}$ (Ln = Eu, Tb, Dy, Sm, Er, Ho) particles. X-ray diffraction (XRD), field emission scanning electron microscopy (FE-SEM), transmission electron microscopy (TEM), photoluminescence (PL), and cathodoluminescence spectra as well as lifetimes were used to characterize the resulting $SiO_2@RE_2O_3$ (RE = rare earth elements) and $SiO_2@Gd_2O_3:Ln^{3+}$ (Eu^{3+}, Tb^{3+}, Dy^{3+}, Sm^{3+}, Er^{3+}, Ho^{3+}) samples. The obtained core-shell phosphors have perfect spherical shape with narrow size distribution (average size ca. 380 nm), smooth surface and non-agglomeration. The thickness of shells could be easily controlled by changing the number of deposition cycles (40 nm for two deposition cycles). Under the excitation of ultraviolet, the Ln^{3+} ion mainly shows its characteristic emissions in the core-shell particles from $Gd_2O_3:Ln^{3+}$ (Eu^{3+}, Tb^{3+}, Sm^{3+}, Dy^{3+}, Er^{3+}, Ho^{3+}) shells.

1. Introduction

Recently, rare-earth functional material have been interestingly studied due to their unique physical and chemical properties and potential applications in the fields of luminescence devices, optical transmission, biochemical probes, medical diagnostics, and so forth [1–7]. For rare-earth oxides, one of the most important family of rare-earth materials, a variety of approaches have been employed such as pyrolyzing their oxysalt precipitates (oxalate, hydroxide, etc.) at high temperatures [8], thermolysis of various rare-earth complexes (acetylacetonates, benzoylacetonates, and acetates) [9], solution combustion synthesis [10], sol–gel method [11], spray pyrolysis [12], etc.

For the core-shell structured particles, the structure, size and composition can be easily altered in a controllable way to tailor their functions [13]. Core-shell structured particles can preserve their unique magnetic, optical, and electronic properties when the surface of the nanoparticles is coated with silica [14,15]. In particular, silica cores with silver and gold shells are the most widely studied due to the potential applications of gold and silver nanoparticles in areas ranging from catalysis and optical devices to immunoassay labeling and surface enhanced Raman spectroscopy (SERS) [16–18]. By using silica spheres as a core and functional material particles (metal oxide, metal,) as the shell, a broad range of hybrid materials with novel properties may result [19]. Silica spheres encapsulated in titania have been investigated as photocatalysts [20] and photonic devices [21], as these can be prepared prescriptively with respect to the size and composition of the support (core) and the coating thickness (shell). Magnetic microspheres consisting of an iron oxide core and silica shell have attracted particular attention for their unique magnetic responsivity, low cytotoxicity, and chemically modifiable surface. The core-shell magnetic silica microspheres have shown great potential in bioseparation, enzyme immobilization, diagnostic analysis, and so on [22]. Spherical SiO_2 particles have been coated with rare-earth functional material layers, by a Pechini sol–gel process. The advantages of the core-shell structured phosphors prepared by this process include the easy availability of homogeneous spherical morphology in different size, decreased cost and its wide practicality for other phosphor materials [23].

Many routes have been explored to fabricate such core-shell particles, such as using co-precipitation [24], layer-by-layer self-assembly [25], surface reaction [26], sol–gel process [27] and MOCVD [28], etc. In most cases, however, the degree of surface coverage is low and the coating is not uniform. The sol–gel process is an effective method for preparing such materials since the reactants can be homogeneously mixed at molecular level in solution. In most of the above cases, the sol–gel precursors used are metal alkoxides and/or organmetallic compounds, which suffer from high cost, toxicity, and difficulty in controlling the

* Corresponding author.
E-mail address: jlin@ciac.jl.cn (J. Lin).

0022-4596/$ - see front matter © 2009 Elsevier Inc. All rights reserved.
doi:10.1016/j.jssc.2009.07.033

experimental processes. An alternative approach to form nanocrystalline thin film is the Pechini-type sol–gel process, which mainly employs the inorganic salts as precursors, citric acid as a chelate ligand, and poly(ethylene glycol) (PEG) as a cross-linking agent [29].

The particle size of rare earth powder directly determines its application effects. Different particle size of powder materials can be used to prepare different requirements of ceramics materials, fluorescent materials, electronic materials, and so on. With this solid-state reaction method, it is quite hard to obtain monodisperse and non-aggregated RE_2O_3 particles. It is well known that monodisperse and spherical silica particles in the nano- to submicron range can be prepared by the hydrolysis and condensation of tetraethoxysilane (TEOS) catalyzed by ammonia [30]. If the silica spheres are coated with phosphors layers, a kind of core/shell phosphor material with spherical morphology will be obtained and the size of the phosphor particles can be controlled by the silica cores.

Here in this work, we developed a large-scale and facile method to obtain monodisperse and spherical core-shell structured $SiO_2@RE_2O_3$ (RE = rare earth elements) and $SiO_2@Gd_2O_3:Ln^{3+}$ (Ln = Eu, Tb, Dy, Sm, Er, Ho) samples by functionalization of silica spheres with RE_2O_3 and $Gd_2O_3:Ln^{3+}$ (Eu^{3+}, Tb^{3+}, Dy^{3+}, Sm^{3+}, Er^{3+}, Ho^{3+}) layers via sol–gel process, and characterize the structure, morphology, photoluminescent and cathodoluminescence properties of the resulting samples in detail.

2. Experiment

2.1. Materials

The starting materials used in the experiments were tetraethoxysilane (TEOS, 99%, Beijing Beihua Chemicals Co., Ltd), Y_2O_3, La_2O_3, Nd_2O_3, Sm_2O_3, Eu_2O_3, Gd_2O_3, Tb_4O_7, Dy_2O_3, Ho_2O_3, Er_2O_3, Tm_2O_3, Yb_2O_3 and Lu_2O_3 (all with purity ≥ 99.99%, Changchun Applied Chemistry Science and Technology Limited, China), $Ce(NO_3)_3 \cdot 6H_2O$ (99.99%, Shanghai Yuelong Nonferrous Metals Ltd), NH_4OH (25 wt%, analytical reagent = A.R., Beijing Beihua Chemicals Co., Ltd), HNO_3 (A.R., Beijing Beihua Chemicals Co., Ltd), polyethylene glycol (PEG, molecular weight = 10 000, A.R., Beijing Beihua Chemicals Co., Ltd), citric acid (A.R., Beijing Beihua Chemicals Co., Ltd) and ethanol (A.R., Beijing Beihua Chemicals Co., Ltd).

2.2. Synthesis of silica cores

The highly monodisperse spheres of silica in the size range of 300–330 nm were synthesized by the well-known Stböer process [30]. This process produces the silica particles with a narrow size distribution in the sub-micrometer range, and the particle size depends on relative concentration of the reagent. In the current work, 0.17 mol/L of TEOS (99 wt%, analytical reagent, A.R.), 7.5 mol/L of deionized H_2O, and 1 mol/L of NH_4OH (25 wt%, A.R.) were added into absolute ethanol and stirred at room temperature for 5 h, resulting in the formation of white silica colloidal suspension. The silica particles were centrifugally separated from the suspension and washed with ethanol three times.

2.3. Coating of SiO_2 cores with RE_2O_3 and $Gd_2O_3:Ln^{3+}$ shells

The core-shell $SiO_2@RE_2O_3$ and $SiO_2@Gd_2O_3:Ln^{3+}$particles were prepared by a Pechini sol–gel process [29,31]. The doping concentration of Ln^{3+} (Ln = Eu, Tb, Dy, Sm, Er, Ho) are 5, 2, 0.5, 0.5, 1, and 1 mol% that of Gd^{3+} in Gd_2O_3 host, respectively, which has been optimized previously [32,33]. Stoichiometric amounts of La_2O_3, Nd_2O_3, Sm_2O_3, Eu_2O_3, Gd_2O_3, Tb_4O_7, Dy_2O_3, Ho_2O_3, Er_2O_3, Tm_2O_3, Yb_2O_3, $Ce(NO_3)_3 \cdot 6H_2O$ and Lu_2O_3, were dissolved in nitric acid, HNO_3, then mixed with a water–ethanol (V/V = 1:7) solution containing citric acid which acted as chelating agent for the metal ions. The molar ratio of metal ions to citric acid was 1:2. Then polyethylene glycol (PEG, molecular weight = 10 000, A.R.) was added with a final concentration of 0.10 g/mL. The solution was stirred for 2 h to form sols, and then the above silica particles were added under stirring. After stirring for another 5 h, the suspension was separated by centrifugation. The particles were dried at 100 °C immediately and then annealed to 700 °C with a heating rate of 120 °C/h and held for 2 h. The above process was repeated several times to increase the thickness of the RE_2O_3 and $Gd_2O_3:Ln^{3+}$ shells on the SiO_2 surface. In this way core-shell structured $SiO_2@RE_2O_3$ and $SiO_2@Gd_2O_3:Ln^{3+}$ particles were obtained.

2.4. Characterizations

The X-ray diffraction (XRD) of the samples was examined on a Rigaku-Dmax 2500 diffractometer using Cu$K\alpha$ radiation (λ = 0.15405 nm). The sample morphologies were inspected using a field emission scanning electron microscope (FESEM, XL30, Philips) and a transmission electron microscope (TEM, JEOL-2010, 200 kV) and high-resolution TEM (HRTEM) (FEI Tecnai G2 S-Twin transmission electron microscope) with a field emission gun operating at 200 kV. The photoluminescence (PL) spectra were taken on a Hitachi F-4500 spectrofluorimeter equipped with a 150 W xenon lamp as the excitation source. The cathodoluminescent (CL) measurements were carried out in an ultra-high-vacuum chamber ($<10^{-8}$ Torr), where the samples were excited by an electron beam at a voltage range of 1–5 kV with different filament currents, and the spectra were recorded on an F-4500 spectrophotometer. The luminescence decay curves were obtained from a Lecroy Wave Runner 6100 Digital Osilloscope (1 GHz) using a tunable laser (pulse width = 4 ns, gate = 50 ns) as the excitation (Contimuum Sunlite OPO). All the measurements were performed at room temperature (RT).

3. Results and discussion

3.1. Formation and morphology of the core-shell particles

The formation and morphological properties of the core-shell $SiO_2@RE_2O_3$ and structured samples were characterized by XRD, SEM and TEM techniques, respectively.

3.1.1. XRD

Fig. 1 shows the XRD patterns of all the considered core-shell $SiO_2@RE_2O_3$ (RE = rare earth elements) samples annealed at 700 °C. For the $SiO_2@RE_2O_3$ (RE = rare earth elements) core-shell particles annealed at 700 °C, apart from the broad band from amorphous SiO_2 ($2\theta = 22.00^\circ$), all diffraction peaks can be well indexed to the pure cubic phase of RE_2O_3 [space group: $Ia\bar{3}$(206)]. This indicates that layer of RE_2O_3 has crystallized well on the surface of amorphous silica spheres. No other phase is detected, suggesting that no reaction occurred between the SiO_2 cores and the RE_2O_3 shells annealing at 700 °C. In general, the nanocrystallite size can be estimated from the Scherrer formula: $D_{hkl} = K\lambda/(\beta \cos\theta)$, where λ is the X-ray wavelength (0.15405 nm), β is the full-width at half-maximum, θ is the diffraction angle, K is a constant (0.89) and D_{hkl} means the size along (hkl) direction.

Here we take diffraction data along the (222), (400) and (440) planes to calculate the size of the nanocrystallites, and the estimated average crystallite sizes of RE_2O_3 on the SiO_2 surface are collected in Table 1. In the Pechini process, the citric acid first formed chelates with RE^{3+}, then the left carboxylic acid groups in the citric acid reacted with polyethylene glycol to form polyester with a suitable viscosity. The Stöber process-derived silica particles contained large amount of free hydroxyl groups (–OH) and silanol groups (Si–OH) on their surface [34]. By stirring silica particles in the solution, a lot of RE^{3+} were absorbed onto the silica particles by physical and chemical interactions. After drying and annealing process, $SiO_2@RE_2O_3$ core-shell particles are produced.

3.1.2. FESEM and TEM

The FESEM micrographs of some typical samples for the as-formed silica particles (a), 700 °C annealed $SiO_2@Gd_2O_3$ core-shell particles (b), $SiO_2@Eu_2O_3$ core-shell particles (c), and $SiO_2@Er_2O_3$ core-shell particles (d) are shown in Fig. 2, respectively. Obviously, the as-formed SiO_2 sample consists of well separated spherical particles with an average size of 300 nm and a narrow size distribution (Fig. 2(a)). After being coated with RE_2O_3 (some typical samples for Gd_2O_3, Eu_2O_3, and Er_2O_3) layers (two times), the resulted core-shell $SiO_2@RE_2O_3$ particles still keep the morphological properties of the core silica particles, i.e., these particles are still spherical and non-aggregated, but slightly larger than the pure silica particles due to the additional layers of RE_2O_3 on them, as shown in Fig. 2(b)–(d), respectively.

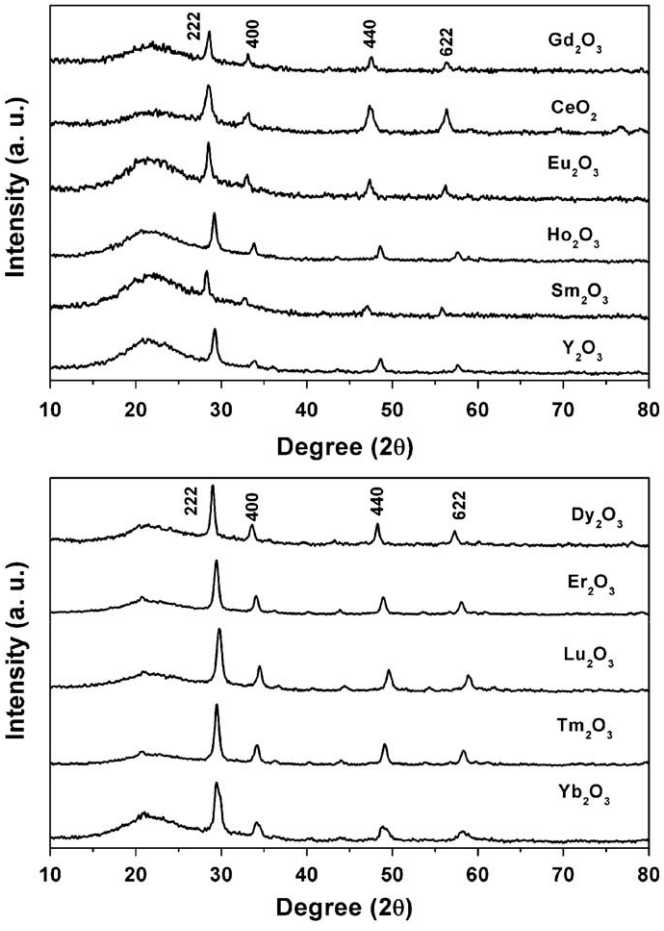

Fig. 1. X-ray diffraction patterns for the $SiO_2@RE_2O_3$ (RE = Y, La, Ce, Nd, Sm, Eu, Gd, Dy, Ho, Er, Tm, Yb, Lu) core-shell particles annealed at 700 °C Miller indices of diffracting lattice planes are also shown.

In order to see the core-shell structure for $SiO_2@Gd_2O_3$ particles, TEM measurements were representatively performed on 300 nm silica particles coated by two times of Gd_2O_3 layer, as shown in Fig. 3(a). The TEM micrographs for the as-formed silica particles are shown Fig. 3(b). In Fig. 3 for the general TEM image, the core-shell structure can be observed clearly due to the different electron penetrability for cores and shells. The cores are black spheres with an average size of 300 nm (in diameter), and the shells have gray color with an average thickness of 40 nm. After being coated two (Fig. 3(a)) layer of Gd_2O_3, the mean size of the resulted $SiO_2@Gd_2O_3$ particles is about 380 nm which is larger than pure silica particles due to the additional layers of Gd_2O_3 on them.

From the HRTEM image of $SiO_2@Gd_2O_3$ (Fig. 3(c)), we can see crystalline phase (Gd_2O_3) with well-resolved lattice fringes. The distance (0.3108 nm) between the adjacent lattice fringes just corresponds to the interplanar distance of Gd_2O_3 (222) planes, agreeing well with the d (222) spacing of the literature value (0.3123 nm) (JCPDS no. 65-3181).The electron diffraction pattern (Fig. 3(d)) indicates that the shells are crystalline (Gd_2O_3 as evidenced by XRD).

Due to the reaction of Gd^{3+}, Ln^{3+} ions on silica surface at high temperature (700 °C), the Gd_2O_3:Ln^{3+} layer are formed. In the Pechini process, the citric acid first formed chelate complexes with Gd^{3+} and Ln^{3+}, then the left carboxylic acid groups in the citric acid reacted with polyethylene glycol to form polyester with a suitable viscosity. The Stöber process-derived silica particles contained large amount of free hydroxyl groups (–OH) and silanol groups (Si–OH) on their surface. By stirring silica particles in the solution, a lot of Gd^{3+} and Ln^{3+} were absorbed onto the silica particles by physical and chemical interactions. After drying and annealing process, $SiO_2@Gd_2O_3$:Ln^{3+} core-shell particles are formed.

3.2. Luminescent properties of $SiO_2@Gd_2O_3$:Ln^{3+} particles

3.2.1. Photoluminescence properties

Our experimental results and previous investigations have shown that cubic Gd_2O_3 is a good host lattice for the luminescence of various optically active lanthanide ions, just like the same type of Y_2O_3. Accordingly, we mainly focus on the luminescence properties of Eu^{3+}, Tb^{3+}, Dy^{3+}, Sm^{3+}, Er^{3+}, and Ho^{3+} in the $SiO_2@Gd_2O_3$:Ln^{3+} (Eu^{3+}, Tb^{3+}, Dy^{3+}, Sm^{3+}, Er^{3+}, Ho^{3+}) core-shell samples, in an effort to reveal that Pechini sol–gel process followed by post-calcining process is an efficient process for the preparation of this kind of oxide phosphors. The doping concentrations of Ln^{3+} in $SiO_2@Gd_2O_3$:Ln^{3+} (Eu^{3+}, Tb^{3+}, Dy^{3+}, Sm^{3+}, Er^{3+}, Ho^{3+}) core-shell samples host discussed in the following parts have been optimized in our experiments.

Table 1
Crystallite sizes of RE_2O_3 in $SiO_2@RE_2O_3$ (RE = Y, La, Ce, Nd, Sm, Eu, Gd, Dy, Ho, Er, Tm, Yb, Lu) core-shell particles annealed at 700 °C.

	Sample ($SiO_2@RE_2O_3$ core-shell particles)										
	Eu_2O_3	Dy_2O_3	Er_2O_3	Gd_2O_3	Ho_2O_3	Lu_2O_3	Tm_2O_3	Yb_2O_3	Ce_2O_3	Sm_2O_3	La_2O_3
Crystallite size (nm)	15.9	16.6	15.7	17.1	14.8	13.4	15.4	13.8	16.8	17.4	16.8

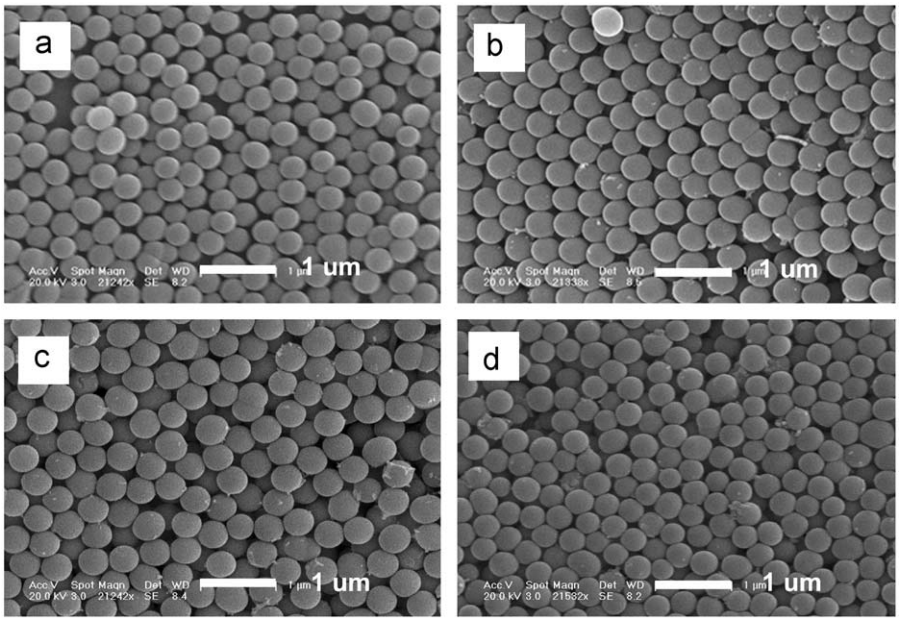

Fig. 2. FESEM micrographs of the as-formed SiO_2 particles (a), 700 °C-annealed SiO_2@Gd_2O_3 core-shell particles (b), SiO_2@Eu_2O_3 core-shell particles (c), and SiO_2@ Er_2O_3 core-shell particles (d), respectively.

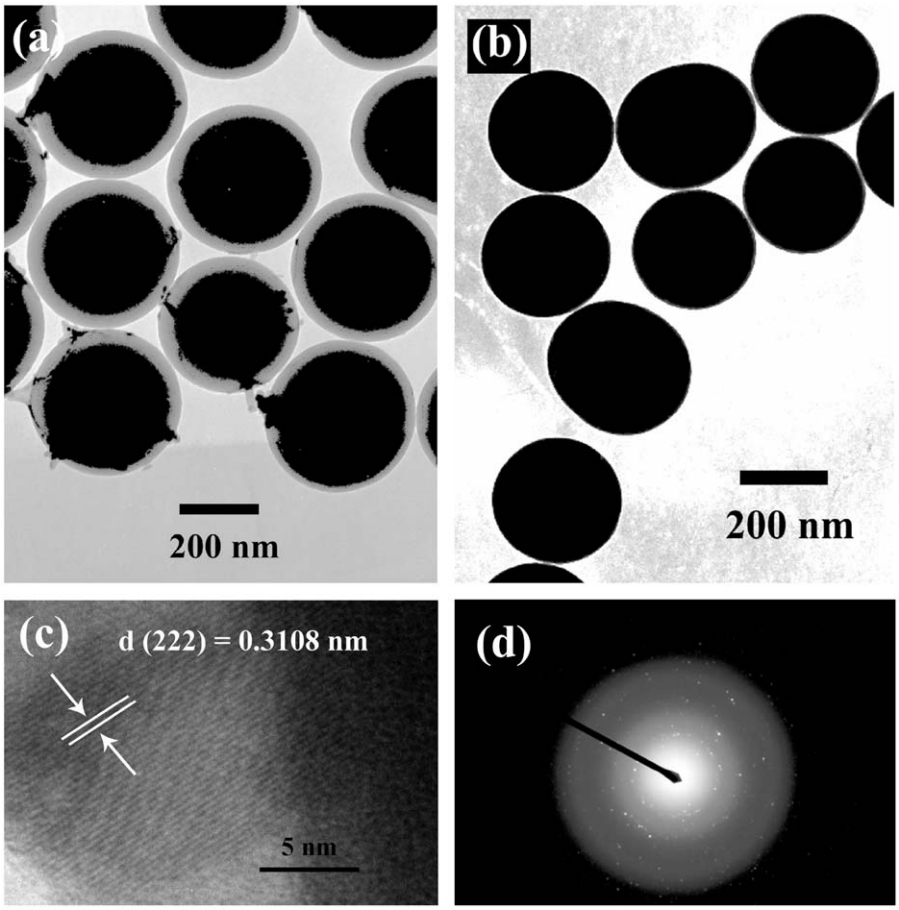

Fig. 3. TEM micrographs for 700 °C-annealed two layer Gd_2O_3-coated SiO_2 particles (a), the as-formed SiO_2 particles (b), high-resolution TEM (c), and the electron diffraction pattern (d) for the sample in (a).

Fig. 4(a)–(f) shows the excitation and emission spectra of SiO_2@Gd_2O_3:Ln^{3+} (Eu^{3+}, Tb^{3+}, Dy^{3+}, Sm^{3+}, Er^{3+}, and Ho^{3+}) samples, respectively. Detailed assignment for the excitation and emission peaks, and luminescent properties (lifetimes, CIE coordinates, and emission colors) are listed in Table 2. All the doped lanthanide ions (Ln^{3+}) show their characteristic transitions within $4f^n$

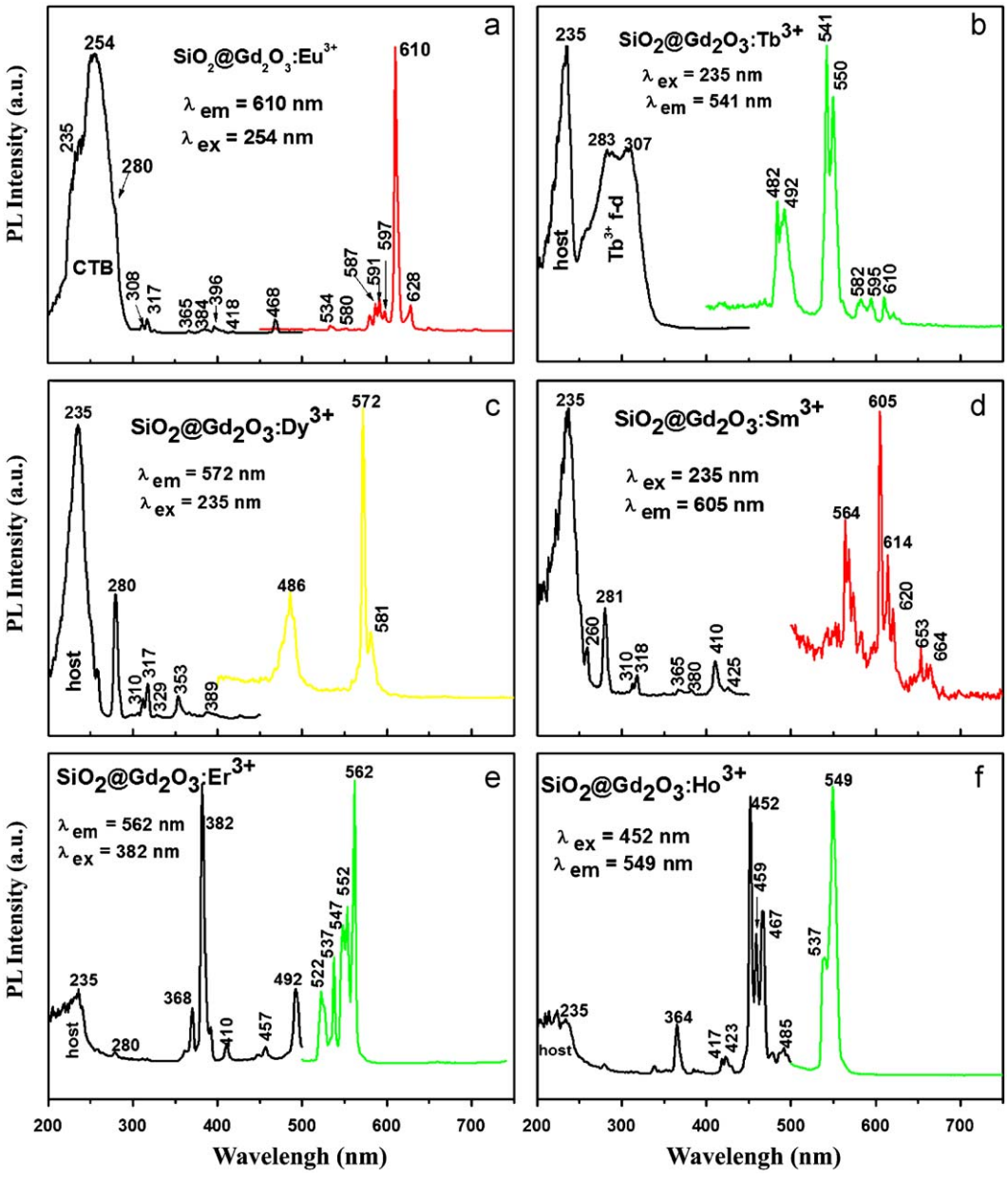

Fig. 4. PL excitation and emission spectra of SiO_2@Gd_2O_3:Ln^{3+} (Ln^{3+} = Eu^{3+}, Tb^{3+}, Dy^{3+}, Sm^{3+}, Er^{3+}, and Ho^{3+}) core-shell samples.

electron configuration in Gd_2O_3 host lattice, with emission colors of red (Eu^{3+}), orange (Sm^{3+}), yellow (Dy^{3+}) and green (Tb^{3+}, Er^{3+}, Ho^{3+}), respectively [35,36]. This can be well demonstrated by the CIE chromaticity diagram. As a representative example, here we only elucidate the case of SiO_2@Gd_2O_3:Dy^{3+} in more detail. Fig. 4(c) exhibits the excitation (left) and emission (right) spectra of the SiO_2@Gd_2O_3:Dy^{3+} sample. The excitation spectrum of Dy^{3+} in SiO_2@Gd_2O_3 core-shell particles monitored with 572 nm emission of Dy^{3+} ($^4F_{9/2}\rightarrow{}^6H_{13/2}$) consists of a strong band from 200 to 270 nm with a maximum at 235 nm can be attribute to the Gd_2O_3 host excitation band and some sharp lines in the longer wavelength region. The excitation lines ^8S–^6I (280 nm), and ^8S–^6P (310 nm, 317 nm) for Gd^{3+} and those *f*–*f* transitions within Dy^{3+} $4f^9$ configuration have also been observed [37], implying that there exists also an energy transfer from Gd^{3+} to Dy^{3+} in the core-shell SiO_2@Gd_2O_3:Dy^{3+} samples [38]. Basically, these excitation lines can be assigned as the transitions from the $^6H_{15/2}$ ground state to the different excited states of Dy^{3+}, that is, 329 nm ($^6P_{3/2}$), 353 nm ($^6P_{7/2}$), and 389 nm ($^4M_{21/2}$), respectively. Upon excitation into the Gd_2O_3 host excitation band at 235 nm, the SiO_2@Gd_2O_3:Dy^{3+} sample shows a strong yellow luminescence. In the emission spectrum, the characteristic transition lines from the lowest excited $^4F_{9/2}$ level of Dy^{3+} to $^6H_{15/2}$ (486 nm) and $^6H_{13/2}$ (572 and 581 nm) are observed, dominated by the Dy^{3+} $^4F_{9/2}\rightarrow{}^6H_{13/2}$ hypersensitive transition ($\Delta J = 2$), which are strongly influenced by the outside surroundings and can be served as a very efficient and sensitive structural probe [39]. This is because the Dy^{3+} is located at a low symmetry local site (C_2, without inversion center) in the Gd_2O_3 host lattices, just like the well known Eu^{3+} $^5D_0\rightarrow{}^7F_2$ in Gd_2O_3 host and in YVO_4 [40]. The CIE coordinates for the emission spectrum of SiO_2@Gd_2O_3:Dy^{3+} are determined as $x = 0.3765$, $y = 0.4294$, located in the yellow region (point 3 in Fig. 5). The lifetime for $^4F_{9/2}$ (detected at 572 nm for the $^4F_{9/2}\rightarrow{}^6H_{13/2}$ transition) of Dy^{3+} was determined to be 0.40 ms in

Table 2
Summary of the photoluminescence properties of SiO_2@Gd_2O_3:Ln^{3+} (Ln^{3+} = Eu^{3+}, Tb^{3+}, Dy^{3+}, Sm^{3+}, Er^{3+}, and Ho^{3+}) samples.

	Excitation peaks (nm)/transition	Emission peaks (nm)/transition	Lifetime (ms)	CIE coordinates	Color
SiO_2@Gd_2O_3:Eu^{3+}	254/Eu^{3+}–O^{2-} CTB 235/host absorption 280, 308, 317/excitations of Gd^{3+} 365/$^7F_0$–$^5D_4$ 384/$^7F_0$–$^5G_2$ 396/$^7F_0$–$^5L_6$ 418/$^7F_0$–$^5D_3$ 468/$^7F_0$–$^5D_2$	534/$^5D_1$–$^7F_1$ 580/$^5D_0$–$^7F_0$ 587, 591, 597/$^5D_0$–$^7F_1$ 610, 628/$^5D_0$–$^7F_2$ 649/$^5D_0$–$^7F_3$	1.45 ($^5D_0$)	$x = 0.5817$ $y = 0.3638$	Red
SiO_2@Gd_2O_3:Tb^{3+}	235/host absorption 283, 307/excitations of Gd^{3+} 275–340/$4f^8$–$4f^75d^1$	482, 492/$^5D_4$–$^7F_6$ 541, 550/$^5D_4$–$^7F_5$ 582, 595/$^5D_4$–$^7F_4$ 610/$^5D_4$–$^7F_3$	1.46 ($^5D_4$)	$x = 0.2815$ $y = 0.5822$	Green
SiO_2@Gd_2O_3:Dy^{3+}	235/host absorption 280, 310, 317/excitations of Gd^{3+} 329/$^6H_{15/2}$–$^6P_{3/2}$ 353/$^6H_{15/2}$–$^6P_{7/2}$ 389/$^6H_{15/2}$–$^4M_{21/2}$	486/$^4F_{9/2}$–$^6H_{15/2}$ 572, 581/$^4F_{9/2}$–$^6H_{13/2}$	0.40 ($^4F_{9/2}$)	$x = 0.3765$ $y = 0.4294$	Yellow
SiO_2@Gd_2O_3:Sm^{3+}	235/host absorption 281, 310, 318/excitations of Gd^{3+} 365/$^6H_{5/2}$–$^4D_{15/2}$ 380/$^6H_{5/2}$–$^4L_{17/2}$ 410/$^6H_{5/2}$–$^4K_{11/2}$ 425/$^6H_{5/2}$–$^4M_{19/2}$	564/$^4G_{5/2}$–$^6H_{5/2}$ 605, 614/$^4G_{5/2}$–$^6H_{7/2}$ 653, 664/$^4G_{5/2}$–$^6H_{9/2}$	1.27 ($^4G_{5/2}$)	$x = 0.5259$ $y = 0.4018$	Orange
SiO_2@Gd_2O_3:Er^{3+}	235/host absorption 280/excitations of Gd^{3+} 368/$^4I_{15/2}$–$^4G_{7/2}$ 382/$^4I_{15/2}$–$^4G_{11/2}$ 410/$^4I_{15/2}$–$^2H_{9/2}$ 457/$^4I_{15/2}$–$^4F_{5/2}$ 492/$^4I_{15/2}$–$^4F_{7/2}$	522, 537/$^2H_{11/2}$–$^4I_{15/2}$ 552, 562/$^4S_{3/2}$–$^4I_{15/2}$	0.016 ($^4S_{3/2}$)	$x = 0.2500$ $y = 0.6355$	Green
SiO_2@Gd_2O_3:Ho^{3+}	235/host absorption 280/excitations of Gd^{3+} 364/$^5I_8$–$^5G_2$ 385/$^5I_8$–$^5G_4$ 417, 423/$^5I_8$–$^5G_5$ 452, 459/$^5I_8$–$^5F_1$, $^5G_6$ 467/$^5I_8$–$^3K_8$ 485/$^5I_8$–$^5F_2$	537, 549/$^5F_4$, $^5S_2$–$^5I_8$	0.038 ($^5S_2$, $^5F_4$)	$x = 0.2774$ $y = 0.5940$	Green

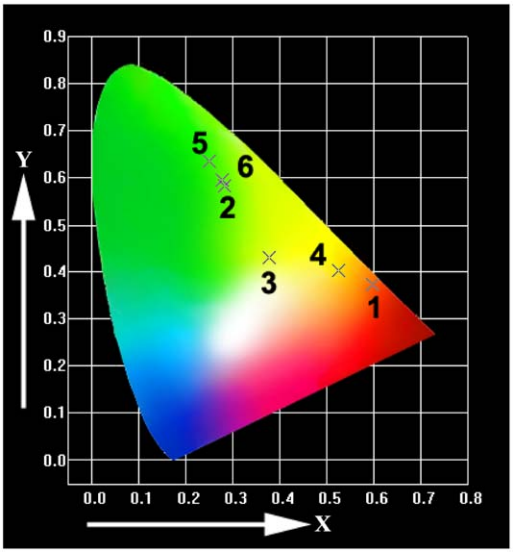

Fig. 5. CIE chromaticity diagram showing the emission colors for SiO_2@Gd_2O_3:Eu^{3+} (**1**), SiO_2@Gd_2O_3:Tb^{3+} (**2**), SiO_2@Gd_2O_3:Dy^{3+} (**3**), SiO_2@Gd_2O_3:Sm^{3+} (**4**), SiO_2@Gd_2O_3:Er^{3+} (**5**), and SiO_2@Gd_2O_3:Ho^{3+} (**6**).

the SiO_2@Gd_2O_3:Dy^{3+} core-shell sample. The photoluminescence properties of other SiO_2@Gd_2O_3:Ln^{3+} (Eu^{3+}, Tb^{3+}, Dy^{3+}, Sm^{3+}, Er^{3+}, and Ho^{3+}) samples can be clearly seen in Table 2 and will not discussed here in more detail.

Finally, it is noted that in all excitation spectra for SiO_2@Gd_2O_3:Ln^{3+} (Eu^{3+}, Tb^{3+}, Dy^{3+}, Sm^{3+}, Er^{3+}, and Ho^{3+}) samples, there is a strong band peaking at 235 nm and some sharp lines at 280 and 317 nm, respectively. Those bands are due to the absorption of the of Gd_2O_3 host lattice and excitation lines of Gd^{3+}. In the SiO_2@Gd_2O_3:Eu^{3+} excitation spectrum, the sharp peaks at 235, and 280 nm superimposed on the CTB of Eu^{3+} can be attribute to the Gd_2O_3 host excitation band [32,33], the ^8S–^6D, and the ^8S–^6I transition lines of Gd^{3+}, respectively [37]. The presence of the Gd_2O_3 host band and Gd^{3+} excitation lines in the excitation spectrum of Eu^{3+} indicates that there exists an energy transfer from the Gd_2O_3 host and Gd^{3+} to the doped Eu^{3+} [41–43]. The excitation spectrum of SiO_2@Gd_2O_3:Tb^{3+} monitored with 543 nm emission of Tb^{3+} ($^5D_4 \rightarrow {}^7F_5$) consists two main features, a strong band from 200 to 273 nm with a maximum at 235 nm and a broad structured plateau with maximum at 283 and 307 nm in the range of 275–340 nm. The former band peaking around 235 nm is related to the fundamental absorption of the host material, the latter structured band located in the range of 275–340 nm should be

assigned to spin-allowed $4f^8$–$4f^7 5d^1$ transitions with maximum at 283 and 307 nm within the Gd^{3+} ion. The luminescence and energy transfer properties provides us an additional proof that the Ln^{3+} ions have successfully entered into the SiO_2@Gd_2O_3 host crystal lattice by Pechini sol–gel, further supporting the XRD analysis.

The PL decay curves for the luminescence of Ln^{3+} in SiO_2@Gd_2O_3:Ln^{3+} (Eu^{3+}/$^5D_0$–$^7F_2$, Tb^{3+}/$^5D_4$–$^7F_5$, Dy^{3+}/$^4F_{9/2}$–$^6H_{13/2}$, Sm^{3+}/$^4G_{5/2}$–$^6H_{7/2}$, Er^{3+}/$^4S_{3/2}$–$^4I_{15/2}$, and Ho^{3+}/$^5F_4$, $^5S_2$–^5I) particles are shown in Fig. 6. These curves can be well fitted by a single exponential function as $I(t) = I_0 \exp(-t/\tau)$ (I_0 is the initial emission intensity at $t = 0$ and τ is the 1/e lifetime of the emission center), and the lifetimes for Ln^{3+} were determined are listed in Table 2, respectively, basically agreeing with the reported lifetime values for Ln^{3+}-doped Gd_2O_3 [32,33].

3.2.2. Cathodoluminescence properties

The cathodoluminescence (CL) properties of the above cubic SiO_2@Gd_2O_3:Ln^{3+} (Ln = Eu, Tb, Dy, Sm, Er, and Ho) core-shell phosphors were also investigated. Fig. 7 shows the typical CL spectra of the SiO_2@Gd_2O_3:Ln^{3+} (Ln = Eu, Tb, Dy, Sm, Er, and Ho) core-shell samples (accelerating voltage = 2 kV; filament current = 92 mA), which are similar to the corresponding PL emission spectra, respectively. The CL emission intensities for the SiO_2@Gd_2O_3:Ln^{3+}(Eu^{3+}, Tb^{3+}, Dy^{3+}, Sm^{3+}, Er^{3+}, and Ho^{3+}) core-shell samples have been investigated as a function of the accelerating voltage and the filament current, as shown in Fig. 8(a) and (b), respectively (Here, we take the SiO_2@Gd_2O_3:Eu^{3+} core-shell sample as example due to similar relation between SiO_2@Gd_2O_3:Ln^{3+} (Ln = Eu, Tb, Dy, Sm, Er, and Ho) samples). When the filament current is fixed at 86 mA, the CL intensity increased with raising the accelerating voltage from 1 to 3 kV (Fig. 8(a)). Similarly, under a 2.0 kV electron beam excitation, the CL intensity also increases with increasing the filament current from 90 to 102 mA (Fig. 8(b)). For cathodoluminescence, the Ln^{3+} ions are excited by the plasma

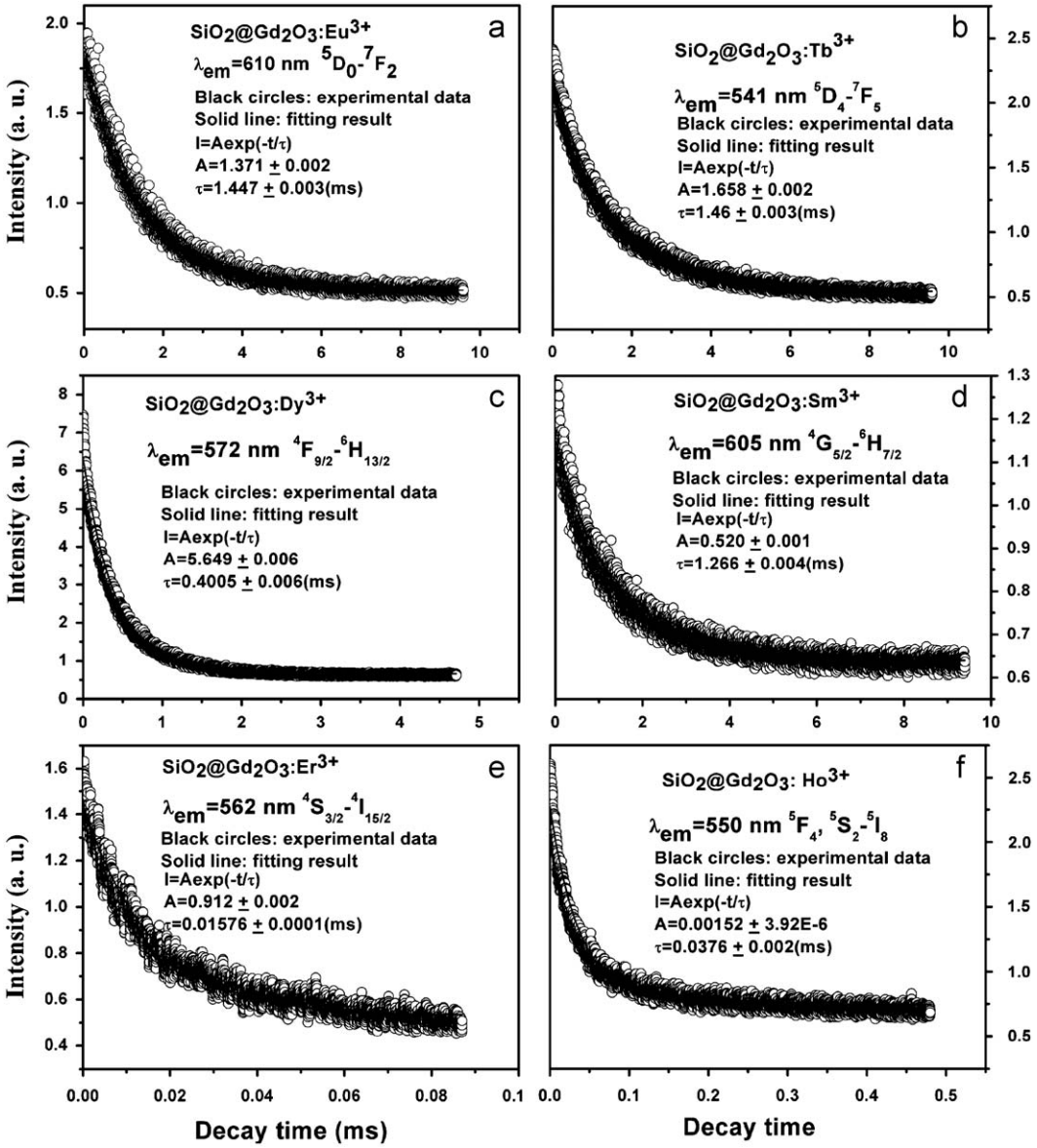

Fig. 6. The decay curves for the $^5D_0$–$^7F_2$ emission of Eu^{3+} (a), the $^5D_4$–$^7F_5$ of emission of Tb^{3+} (b), the $^4F_{9/2}$–$^6H_{13/2}$ of emission of Dy^{3+} (c), the $^4G_{5/2}$–$^6H_{7/2}$ of emission of Sm^{3+} (d), the $^4S_{3/2}$–$^4I_{15/2}$ of emission of Er^{3+} (e), $^5F_4$, $^5S_2$–$^5I_8$ of emission of Ho^{3+} (f) in SiO_2@Gd_2O_3:Ln (Ln = Eu, Tb, Dy, Sm, Er, and Ho) sample annealed at 700 °C (λ_{ex} = 250 nm laser).

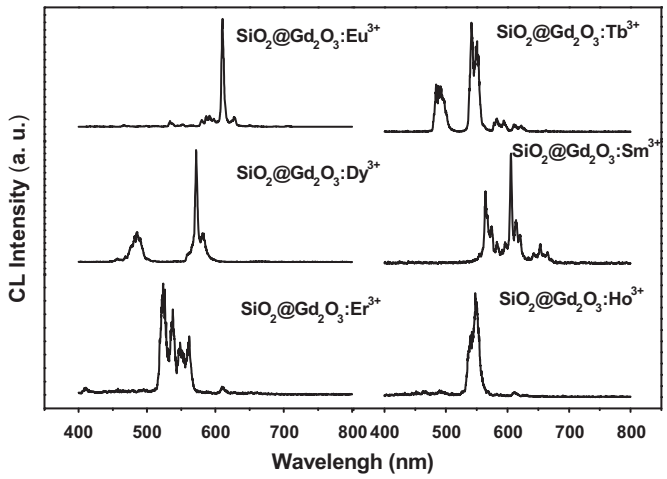

Fig. 7. CL emission spectra of the $SiO_2@Gd_2O_3:Ln^{3+}$ (Ln^{3+} = Eu^{3+}, Tb^{3+}, Dy^{3+}, Sm^{3+}, Er^{3+}, and Ho^{3+}) samples under electron beam excitation with accelerating voltage = 2 kV and filament current = 92 mA.

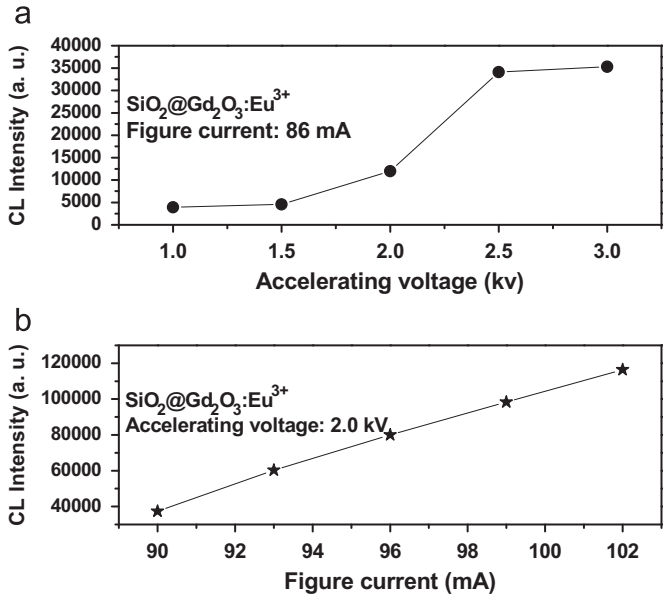

Fig. 8. CL emission intensity of the $SiO_2@Gd_2O_3:Eu^{3+}$ samples as a function of the accelerating voltage (a) and the filament current (b).

produced by the incident electrons. The electron penetration depth can be estimated by

$$L[\text{Å}] = 250(A/\rho)(E/Z^{1/2})n \quad (1)$$

where $n = 1.2/(1–0.29\log_{10}Z)$, A is the atomic or molecular weight of the material, ρ is the bulk density, Z is the atomic number or the number of electrons per molecule in the case compounds, and E is the accelerating voltage (kV) [44]. For $SiO_2@Gd_2O_3:Eu^{3+}$ core-shell sample, the calculated electron penetration depths at 3 kV is about 11.7 nm. With the increase of accelerating voltage, more plasma will be produced by the incident electrons, resulting in more Eu^{3+} being excited and higher CL intensity. The increase in electron energy is attributed to deeper penetration of electron into the phosphor body which is governed by Eq. (1). The deeper penetration of electrons in the phosphor body results in an increase in electron-solid interaction volume in which excitation of Eu^{3+} ions is responsible for the light emission. Therefore, an increase in interaction volume (which effectively determines the generation of light inside the phosphor) with an increase in electron energy brings about an increase in CL brightness of $SiO_2@Gd_2O_3:Eu^{3+}$ core-shell sample [45].

4. Conclusions

Spherical core-shell structured $SiO_2@RE_2O_3$ (RE = rare earth elements) and $SiO_2@Gd_2O_3:Ln^{3+}$ (Eu^{3+}, Tb^{3+}, Dy^{3+}, Er^{3+}, Ho^{3+}, Sm^{3+}) particles with uniform size distribution have been successfully prepared by Pechini sol-gel method followed by annealing at high temperature. Upon UV excitation, the luminescence properties are typical those of $Gd_2O_3:Ln^{3+}$ (Eu^{3+}, Tb^{3+}, Dy^{3+}, Er^{3+}, Ho^{3+}, Sm^{3+}). The advantages of the phosphors prepared by this process are the easy availability of homogeneous spherical morphology in different size, and its wide practicality for other phosphor materials.

Acknowledgments

This project is financially supported by the foundation of "Bairen Jihua" of Chinese Academy of Sciences, the MOST of China (2003CB314707, 2010CB327704), and the National Natural Science Foundation of China (NSFC 50572103, 20431030, 00610227).

References

[1] X. Wang, J. Zhuang, Q. Peng, Y. Li, Nature 437 (2005) 121–124.
[2] Y.C. Cao, J. Am. Chem. Soc. 126 (2004) 7456.
[3] R. Si, Y.W. Zhang, L.P. You, C.H. Yan, Angew. Chem. Int. Ed. 44 (2005) 3256.
[4] T. Yu, J. Joo, Y.I. Park, T. Hyeon, J. Am. Chem. Soc. 128 (2006) 1786.
[5] J.W. Stouwdam, F.C.J.M. van Veggel, Nano Lett. 2 (2002) 733.
[6] K. Kömpe, H. Borchert, J. Storz, A. Lobo, S. Adam, T. Möller, M. Haase, Angew. Chem. Int. Ed. 42 (2003) 5513.
[7] Y.W. Zhang, X. Sun, R. Si, L.P You, C.H Yan, J. Am. Chem. Soc. 127 (2005) 3260.
[8] G.A.M. Hussein, J. Anal, Appl. Pyrolysis 37 (1996) 111.
[9] R. Si, Y.W. Zhang, H.P. Zhou, L.D. Sun, C.H. Yan, Chem. Mater. 19 (2007) 18.
[10] J.A. Capobianco, F. Vetrone, J.C. Boyer, A. Speghini, M. Bettinelli, Opt. Mater. 19 (2002) 259.
[11] H. Guo, Y.F. Li, D.Y. Wang, W.P. Zhang, M. Yin, L.R. Lou, S.D. Xia, J. Alloys Compd. 376 (2004) 23.
[12] W.J. Tobler, W. Durisch, Appl. Energy 85 (2008) 371.
[13] A.E. Neeves, M.H. Birnboim, J. Opt. Soc. Am. B 6 (1989) 787.
[14] Y.H. Deng, D.W. Qi, C.H. Deng, X.M. Zhang, D.Y. Zhao, J. Am. Chem. Soc. 130 (2008) 28.
[15] T. Zhai, Z. Gu, Y. Dong, H. Zhong, Y. Ma, H. Fu, Y. Li, J. Yao, J. Phys. Chem. C 111 (2007) 11604.
[16] K. Aslan, M. Wu, J.R. Lakowicz, C.D. Geddes, J. Am. Chem. Soc. 129 (2007) 1524.
[17] Y. Lu, Y. Yin, Z.Y. Li, Y. Xia, Nano Lett. 2 (2002) 785.
[18] I. Tunc, S. Suzer, M.A. Correa-Duarte, L.M. Liz-Marzan, J. Phys. Chem. B 109 (2005) 7597.
[19] Y. Kobayashi, M.A. Correa-Duarte, L.M. Liz-Marza′n, Langmuir 17 (2001) 6375.
[20] P. Wilhelm, D. Stephan, J. Colloid Interface Sci. 293 (2006) 88.
[21] H. Nakamura, M. Ishii, A. Tsukigase, M. Harada, H. Nakano, Langmuir 22 (2006) 1268.
[22] Y.H. Deng, D.W. Qi, C.H. Deng, X.M. Zhang, D.Y. Zhao, J. Am. Chem. Soc. 130 (2008) 28.
[23] M. Yu, H. Wang, C.K. Lin, G.Z. Li, J. Lin, Nanotechnology 17 (2006) 3245.
[24] H. Giesche, E. Matijević, J. Mater. Res. 9 (1994) 436.
[25] V. Salgueirino-Maceira, M. Spasova, M. Farle, Adv. Funct. Mater. 15 (2005) 1036.
[26] A. Dokoutchaev, J.T. James, S.C. Koene, S. Pathak, G.K.S. Prakash, M.E. Thompson, Chem. Mater. 11 (1999) 2389.
[27] R.A. Caruso, M. Antonietti, Chem. Mater. 13 (2001) 3272.
[28] K.W. Chang, J.J. Wu, Adv. Mater. 17 (2005) 241.
[29] M. Yu, J. Lin, Z. Wang, J. Fu, S. Wang, H.J. Zhang, Y.C. Han, Chem. Mater. 14 (2002) 2224.
[30] W. Stöber, A. Fink, E. Bohn, J. Colloid Interface Sci. 26 (1968) 62.
[31] M.L. Pang, J. Lin, Z.Y. Cheng, J. Fu, R.B. Xing, S.B. Wang, Mater. Sci. Eng. B 100 (2003) 124.
[32] M.L. Pang, J. Lin, J. Fu, R.B. Xing, C.X. Luo, Y.C. Han, Opt. Mater. 23 (2003) 547.
[33] J. Yang, C.X. Li, Z.Y. Cheng, X.M. Zhang, Z.W. Quan, C.M. Zhang, J. Lin, J. Phys. Chem. C 111 (2007) 18148.

[34] Y. Chen, J.O. Iroh, Chem. Mater. 11 (1999) 1218.
[35] W.O. Gordon, J.A. Carter, B.M. Tissue, J. Lumin. 108 (2004) 339.
[36] X.Y. Chen, E. Ma, G.K. Liu, J. Phys. Chem. C 111 (2007) 10404.
[37] G. Blasse, B.C. Grabmaier, Luminescent Materials, Springer, Berlin, 1994.
[38] G.Z. Li, M. Yu, Z.L. Wang, J. Lin, R.S. Wang, J. Fang, J. Nanosci. Nanotechnol. 6 (2006) 1416.
[39] J.M. Nedelec, D. Avignant, R. Mahiou, Chem. Mater. 14 (2002) 651.
[40] M. Yu, J. Lin, J. Fang, Chem. Mater. 17 (2005) 1783.
[41] C. Louis, R. Bazzi, M.A. Flores, W. Zheng, K. Lebbou, O. Tillement, B. Mercier, C. Dujardin, P. Perriat, J. Solid State Chem. 173 (2003) 335.
[42] G.X. Liu, G.Y. Hong, D.X. Sun, J. Colloid Interface Sci. 278 (2004) 133.
[43] M.D. Dramicanin, V. Jokanovic, Z. Andric, Recent Dev. Adv. Mater. Processes 518 (2006) 455.
[44] C. Feldman, Phys. Rev. 117 (1960) 455.
[45] D. Kumar, K.G. Cho, Z. Chen, V. Craciun, P.H. Holloway, R.K. Singh, Phys. Rev. B 60 (1999) 13331.